CrossMark

J. Fluid Mech. (2017), *vol.* 814, *pp.* 165–184. © Cambridge University Press 2017
doi:10.1017/jfm.2017.19

Statistics of kinetic and thermal energy dissipation rates in two-dimensional turbulent Rayleigh–Bénard convection

Yang Zhang[1], **Quan Zhou**[1,†] **and Chao Sun**[2]

[1]Shanghai Institute of Applied Mathematics and Mechanics, and Shanghai Key Laboratory of Mechanics in Energy Engineering, Shanghai University, Shanghai 200072, China

[2]Center for Combustion Energy and Department of Thermal Engineering, Tsinghua University, 100084 Beijing, China

(Received 7 September 2016; revised 3 December 2016; accepted 16 December 2016; first published online 3 February 2017)

We investigate the statistical properties of the kinetic ε_u and thermal ε_θ energy dissipation rates in two-dimensional (2-D) turbulent Rayleigh–Bénard (RB) convection. Direct numerical simulations were carried out in a box with unit aspect ratio in the Rayleigh number range $10^6 \leqslant Ra \leqslant 10^{10}$ for Prandtl numbers $Pr = 0.7$ and 5.3. The probability density functions (PDFs) of both dissipation rates are found to deviate significantly from a log-normal distribution. The PDF tails can be well described by a stretched exponential function, and become broader for higher Rayleigh number and lower Prandtl number, indicating an increasing degree of small-scale intermittency with increasing Reynolds number. Our results show that the ensemble averages $\langle \varepsilon_u \rangle_{V,t}$ and $\langle \varepsilon_\theta \rangle_{V,t}$ scale as $Ra^{-0.18\sim-0.20}$, which is in excellent agreement with the scaling estimated from the two global exact relations for the dissipation rates. By separating the bulk and boundary-layer contributions to the total dissipations, our results further reveal that $\langle \varepsilon_u \rangle_{V,t}$ and $\langle \varepsilon_\theta \rangle_{V,t}$ are both dominated by the boundary layers, corresponding to regimes I_l and I_u in the Grossmann–Lohse (GL) theory (*J. Fluid Mech.*, vol. 407, 2000, pp. 27–56). To include the effects of thermal plumes, the plume–background partition is also considered and $\langle \varepsilon_\theta \rangle_{V,t}$ is found to be plume dominated. Moreover, the boundary-layer/plume contributions scale as those predicted by the GL theory, while the deviations from the GL predictions are observed for the bulk/background contributions. The possible reasons for the deviations are discussed.

Key words: Bénard convection, convection, turbulent flows

1. Introduction

Turbulent Rayleigh–Bénard (RB) convection, which describes the convective motion of a fluid layer between two horizontal parallel plates heated from below and cooled from above, is a typical model system abstracted from many natural phenomena and industrial processes (Ahlers, Grossmann & Lohse 2009; Lohse & Xia 2010; Chillà & Schumacher 2012; Sun & Zhou 2014). A better knowledge of this system not only points out a convenient way of understanding complicated convection problems occurring in nature but also gives fundamental and perspective insight into

† Email address for correspondence: qzhou@shu.edu.cn

https://doi.org/10.1017/jfm.2017.19 Published online by Cambridge University Press

some features of turbulence (Kadanoff 2001). One of the key issues that has been comprehensively investigated is to physically understand the functional form of the global heat transport, measured by the Nusselt number, defined as

$$Nu = \frac{Q}{\chi \varDelta / H}, \tag{1.1}$$

as a function of the two control parameters of the system: the Rayleigh number Ra and the Prandtl number Pr, defined as

$$Ra = \frac{\beta g \Delta H^3}{\nu\kappa} \quad \text{and} \quad Pr = \frac{\nu}{\kappa}. \tag{1.2a,b}$$

Here, Q is the heat current density across the fluid layer of height H for an imposed temperature difference $\varDelta$, g is the acceleration due to gravity and χ, β, ν and κ are the thermal conductivity, thermal expansion coefficient, kinematic viscosity and thermal diffusivity of the convecting fluid, respectively. The quantities that play an important role in the heat-transport processes are the kinetic and thermal energy dissipation rates, which are respectively given by

$$\varepsilon_u(\boldsymbol{x}, t) = \frac{1}{2}\nu \sum_{ij} \left[\frac{\partial u_j(\boldsymbol{x}, t)}{\partial x_i} + \frac{\partial u_i(\boldsymbol{x}, t)}{\partial x_j}\right]^2 \tag{1.3}$$

and

$$\varepsilon_\theta(\boldsymbol{x}, t) = \kappa \sum_i \left[\frac{\partial \theta(\boldsymbol{x}, t)}{\partial x_i}\right]^2. \tag{1.4}$$

These two quantities denote direct dissipation of kinetic and thermal energy due to the effects of the fluid viscosity and thermal diffusivity, and can be quantified by the magnitudes of the gradients of the turbulent velocity and temperature fields, $\boldsymbol{u}(\boldsymbol{x}, t)$ and $\theta(\boldsymbol{x}, t)$. As turbulent RB convection is a typical example for turbulent flows in a closed system, its local dissipation rates can be directly connected to the global heat transport through the convection cell via the two exact relations:

$$\langle \varepsilon_u \rangle_{V,t} = \frac{\nu^3}{H^4}(Nu - 1)RaPr^{-2} \tag{1.5}$$

and

$$\langle \varepsilon_\theta \rangle_{V,t} = \kappa \frac{\varDelta^2}{H^2} Nu, \tag{1.6}$$

where $\langle \cdot \rangle_{V,t}$ denotes an ensemble (or space–time) average. These relations form the backbone of the popular Grossmann–Lohse (GL) theory of turbulent heat transfer (Grossmann & Lohse 2000, 2004).

Due to the difficulty in the measurements of velocity or temperature gradients, the experimental studies on the dissipation rates are rather limited in the field of turbulent RB convection. The first attempt on this subject was carried out by He, Tong & Xia (2007) and He & Tong (2009), who used four identical thermistors to simultaneously measure the three components of the local temperature gradient. The time-averaged thermal energy dissipation rate was then decomposed into two contributions: one comes from the mean temperature gradient that concentrates in the thermal boundary layers (BL) and the other generated by thermal plumes that dominates in the bulk region. Using the same data set, He, Tong & Ching (2010), He, Ching & Tong (2011) further constructed a locally averaged thermal dissipation rate over a time

https://doi.org/10.1017/jfm.2017.19 Published online by Cambridge University Press

interval τ, which was found to exhibit good scaling in τ with exponents being in excellent agreement with those predicted by a phenomenological intermittency model. By measuring the second-order velocity structure functions in the dissipative range, the time-averaged kinetic energy dissipation rate was indirectly obtained at the cell centre by Ni, Huang & Xia (2011). The *Ra* dependence of the measured results was found to agree with the predictions of the GL model and it was shown that local kinetic energy dissipation rate balances local heat flux in the central region of turbulent thermal convection.

Compared with the difficulty in experiments, the direct numerical simulations (DNS) data enable the calculation of dissipation rates. The pioneering work on this subject was performed by Verzicco & Camussi (2003) and Verzicco (2003), who analysed the statistical properties of ε_u and ε_θ in a cylindrical cell of aspect ratio one half. Later, Shishkina & Wagner (2006, 2008) investigated the formation and development of thermal plumes and their interaction via evaluating the thermal dissipation rates. Emran & Schumacher (2008) examined the probability density functions (PDF) of the thermal dissipation rates in a cylindrical cell. They found that, similarly to passive scalar mixing, the PDFs deviate significantly from a log-normal distribution and the PDF tails can be well fitted by a stretched exponential function. Furthermore, Kaczorowski & Wagner (2009) used the PDFs of ε_θ to distinguish the three different physical regions in a long rectangular cell via the two inflection points of the PDFs. Ng *et al.* (2015) calculated in vertical natural convection the dissipation contributions that come from respectively the BL and bulk regions, and their results revealed that the contributions scale as those predicted by the GL theory. Recently, Petschel *et al.* (2013, 2015) put forward the idea of dissipation layers, which are based on the systematic measurements of the dissipation rates and were found to share central characteristics with classical BLs. In addition, such dissipation layers can be extended naturally to arbitrary boundary conditions.

In the paper, we provide a detailed statistical analysis of the kinetic and thermal energy dissipation rates in two-dimensional (2-D) turbulent RB convection by means of the DNS data for $10^6 \leqslant Ra \leqslant 10^{10}$ and for $Pr = 0.7$ and 5.3. Two considerations prompted us to restrict ourselves to the 2-D geometry: (i) the numerical effort required for 2-D simulations is much smaller so that a good resolution of the BLs as well as of the dissipation events at high Rayleigh/Reynolds numbers is guaranteed and systematic studies can be performed; (ii) many well-cited theories for turbulent RB systems are essentially two-dimensional, e.g. the popular GL theory (Grossmann & Lohse 2000) and the recent Whitehead–Doering theory for the ultimate regime (Whitehead & Doering 2011).

The remainder of this paper is organized as follows. In § 2, we give a brief description of the governing equations and numerical model. The numerical results are presented and analysed in § 3, which is divided into four parts. Section 3.1 describes the global features of the simulations. Section 3.2 studies PDFs of ε_u and ε_θ. In § 3.3, we compare the dissipation contributions coming from the bulk with those coming from the BL regions. The *Ra* and *Re* dependences of $\langle\varepsilon_u\rangle$ and $\langle\varepsilon_\theta\rangle$ are presented and discussed in § 3.4. Finally, we summarize our findings in § 4.

2. Numerical methods

The mathematical model and the numerical scheme have been described in detail elsewhere (Huang & Zhou 2013; Zhou 2013; Qiu, Liu & Zhou 2014; Zhou *et al.* 2016) and thus we give only their main features here. The computational domain

https://doi.org/10.1017/jfm.2017.19 Published online by Cambridge University Press

consists of a 2-D box with uniform grids and of unit aspect ratio (i.e. ratio of the horizontal length L to the cell height H, $\Gamma = L/H = 1$). While the two vertical side walls are chosen to be adiabatic, cold and hot fixed temperatures, $\theta = -0.5$ and 0.5, are applied to the top and bottom plates, respectively. All the solid surfaces satisfy the no-penetration and no-slip velocity boundary conditions.

The flow is solved by the numerical integration of the 2-D time-dependent Navier–Stokes equations in vorticity–streamfunction formulation under the Boussinesq approximation. The numerical scheme is a compact fourth-order central finite-difference method (Liu, Wang & Johnston 2003). The equations are given by

$$\frac{\partial \omega}{\partial t} + (\boldsymbol{u} \cdot \nabla)\omega = \nu \nabla^2 \omega + \frac{\partial \theta}{\partial x}, \tag{2.1}$$

$$\nabla^2 \psi = \omega, \tag{2.2}$$

$$u = -\frac{\partial \psi}{\partial z}, \quad w = \frac{\partial \psi}{\partial x}, \tag{2.3a,b}$$

$$\frac{\partial \theta}{\partial t} + (\boldsymbol{u} \cdot \nabla)\theta = \kappa \nabla^2 \theta, \tag{2.4}$$

where u and w are, respectively, the horizontal and vertical components of the velocity field, ψ is the streamfunction and $\omega = \partial w/\partial x - \partial u/\partial z$ is the vorticity field. The equations have been made non-dimensional by using the cell height H, the temperature difference Δ and the free-fall velocity $U = \sqrt{\beta g \Delta H}$, and hence the corresponding fluid viscosity $\nu = \sqrt{Pr/Ra}$ and thermal diffusivity $\kappa = \sqrt{1/PrRa}$. In our present study, the Rayleigh number was varied from 10^6 to 10^{10}, while the Prandtl number was fixed at $Pr = 0.7$ and 5.3, respectively corresponding to the working fluids of air (du Puits, Resagk & Thess 2007) and water at 31° (Zhou *et al.* 2012). In table 1, we list the flow and grid parameters of the simulations.

We briefly comment on the spatial and temporal resolutions. For the numerical study of turbulent RB convection, the mesh size must be set to achieve a full resolution of the BLs (Shishkina *et al.* 2010), as well as to resolve the smallest scales of the flow, these being the dissipative scales, i.e. the Kolmogorov scale η and the Batchelor scale η_B. In the present study, the number of grid points was generally chosen to be the same for the two different Pr, except for the highest Rayleigh number $Ra = 10^{10}$, and was increased from 129×129 to 3073×3073 for Ra increasing from 10^6 to 10^{10}. In table 1, we list the number of grids N_{BL} within the thermal BL and the grid spacing Δ_g is compared with η and η_B for each simulation. It is seen that for all of our simulations the thermal BL is resolved with at least 10 grid points and the grid spacing $\Delta_g \lesssim 0.57\eta$ and $\Delta_g \lesssim 0.48\eta_B$. Furthermore, the uniform grids adopted in the present study ensure the spatial resolution at the side walls to be the same as that close to the top and bottom plates. The viscous BLs near both the plates and side walls are resolved with at least 8 grid points at lower Pr and with at least 16 grid points at higher Pr, due to the increasing viscous BL thickness with increasing Pr. To check whether the present temporal resolution resolves the smallest time scale in turbulence, we also compare the simulation time interval Δ_t with the Kolmogorov time scale τ_η in table 1. One sees that $\Delta_t/\tau_\eta < 0.01$ for all runs, thus guaranteeing the adequate temporal resolution. We note that the present spatial resolutions also obey the criterion proposed by Grötzbach (1983) and the time step Δ_t is chosen to fulfil the Courant–Friedrichs–Lewy (CFL) conditions, i.e. the CFL number is 0.3 or less for all computations presented in this paper.

Another way to verify the grid resolution is to test whether the two global exact relations (1.5) and (1.6) hold for the simulations, as suggested by Stevens, Verzicco

https://doi.org/10.1017/jfm.2017.19 Published online by Cambridge University Press

Pr	Ra	$N_x \times N_z$	Nu	Re	$\frac{\langle \varepsilon_u \rangle_{V,t}}{(Nu-1)/\sqrt{RaPr}}$	$\frac{\langle \varepsilon_\theta \rangle_{V,t}}{Nu/\sqrt{RaPr}}$	N_{BL}	$\frac{\Delta_g}{\eta}$	$\frac{\Delta_g}{\eta_B}$	$\frac{\Delta_t}{\tau_\eta}$
0.7	1×10^6	129×129	6.30	279	1.0041	1.0023	11	0.45	0.37	0.0069
0.7	3×10^6	193×193	7.64	492	1.0038	1.0018	13	0.42	0.35	0.0062
0.7	1×10^7	257×257	11.37	968	1.0031	1.0014	12	0.47	0.39	0.0058
0.7	3×10^7	385×385	16.50	1800	1.0025	1.0006	12	0.46	0.38	0.0071
0.7	1×10^8	513×513	25.25	3662	1.0021	0.9998	11	0.52	0.43	0.0088
0.7	3×10^8	769×769	35.73	6897	1.0017	1.0006	11	0.50	0.42	0.0070
0.7	1×10^9	1025×1025	53.51	15101	0.9967	0.9996	10	0.56	0.47	0.0069
0.7	3×10^9	1537×1537	66.95	28418	0.9896	1.0013	12	0.52	0.43	0.0029
0.7	1×10^{10}	2049×2049	93.88	61797	1.0358	0.9996	12	0.57	0.48	0.0023
5.3	1×10^6	129×129	6.87	38	1.0026	1.0019	10	0.17	0.38	0.0042
5.3	3×10^6	193×193	9.33	70	1.0022	1.0009	11	0.16	0.37	0.0038
5.3	1×10^7	257×257	13.28	156	1.0017	1.0008	10	0.18	0.41	0.0023
5.3	3×10^7	385×385	18.86	296	1.0010	1.0009	11	0.17	0.40	0.0037
5.3	1×10^8	513×513	26.21	596	1.0000	1.0002	10	0.19	0.44	0.0033
5.3	3×10^8	769×769	35.96	1145	1.0016	1.0001	11	0.18	0.42	0.0026
5.3	1×10^9	1025×1025	51.28	2269	1.0030	1.0005	11	0.20	0.46	0.0031
5.3	3×10^9	1537×1537	71.57	4330	0.9996	1.0019	11	0.19	0.44	0.0022
5.3	1×10^{10}	3073×3073	103.0	9916	0.9963	1.0003	15	0.16	0.33	0.0013

TABLE 1. Simulation parameters. The columns from left to right indicate the following: Pr, Ra, the resolution in horizontal and vertical directions $N_x \times N_z$, Nu, $Re = U_{rms}H/\nu$ with $U_{rms} = \sqrt{\langle (u^2 + w^2) \rangle_{V,t}}$, $\langle \varepsilon_u \rangle_{V,t}$ compared with that obtained from the exact relation $\langle \varepsilon_u \rangle = \nu^3/H^4(Nu-1)RaPr^{-2} = (Nu-1)/\sqrt{RaPr}$, $\langle \varepsilon_\theta \rangle_{V,t}$ compared with that obtained from the exact relation $\langle \varepsilon_\theta \rangle = \kappa \Delta^2/H^2 Nu = Nu/\sqrt{RaPr}$, the number of grid points within the thermal BL N_{BL}, the grid spacing Δ_g compared with the Kolmogorov scale estimated by the global criterion $\eta = HPr^{1/2}/[Ra(Nu-1)]^{1/4}$, Δ_g compared with the Batchelor scale $\eta_B = \eta Pr^{-1/2}$ (Silano, Sreenivasan & Verzicco 2010), the time interval Δ_t compared with the Kolmogorov time scale $\tau_\eta = \sqrt{\nu/\langle \varepsilon_u \rangle} = \sqrt{Pr/(Nu-1)}$.

& Lohse (2010). The sixth and seventh columns of table 1 compare the directly calculated dissipation rates with those obtained from Ra, Pr and Nu via the exact relations. One sees that for most of the cases the difference is less than 1 %. This guarantees the adequate resolution for small-scale turbulent structures, like thermal plumes, even in the regions very close to the horizontal plates and close to the vertical side walls.

3. Results and discussion

3.1. *Global features*

In figures 1(*a,b*), we show typical examples of the instantaneous velocity fields (arrows), overlapped with the corresponding temperature fields (colour), obtained from the simulations with $Ra = 10^{10}$ and with $Pr = 0.7$ and 5.3, respectively. As shown in figure 1(*b*), the overall flow pattern consists of a large counter-clockwise (or clockwise in some cases) rotatory motion in the bulk and several smaller secondary rolls at the four corners. This flow pattern is the same as those observed in previous studies (Sugiyama *et al.* 2009, 2010; Zhou *et al.* 2011; Chandra & Verma 2013) and is found to be stable for most of the time and for most of the runs, except for the simulation with $Ra = 10^{10}$ and $Pr = 0.7$, where the corner-flow rolls are always not stable and would detach from the corners (see figure 1*a*).

https://doi.org/10.1017/jfm.2017.19 Published online by Cambridge University Press

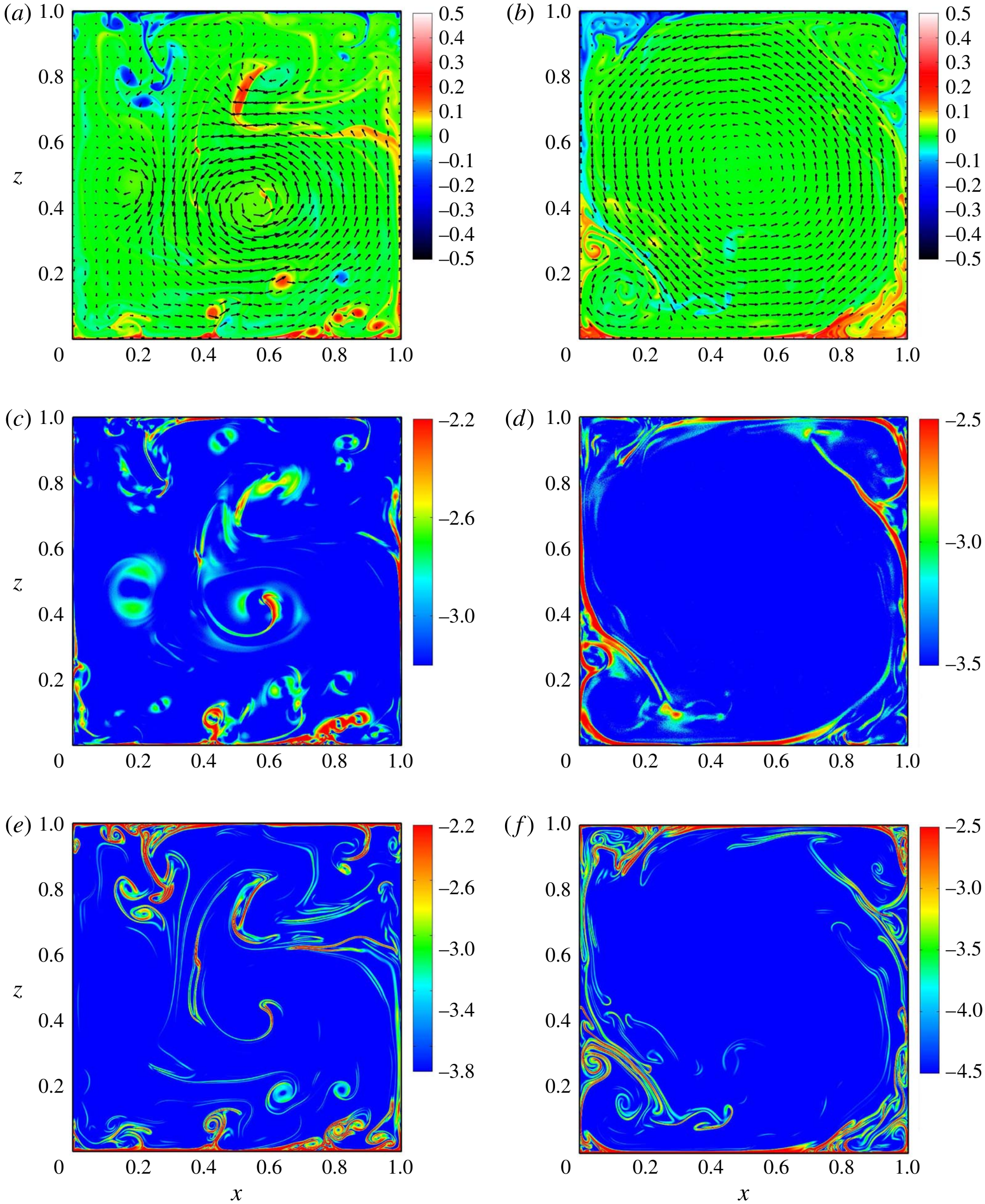

FIGURE 1. (*a*,*b*) Typical snapshots of the instantaneous temperature (colour) and velocity (arrows) fields for $Ra=10^{10}$ and for $Pr=0.7$ (*a*) and 5.3 (*b*). (*c*–*f*) The corresponding logarithmic fields of kinetic $\log_{10}\varepsilon_u(x,z)$ (*c*,*d*) and thermal $\log_{10}\varepsilon_\theta(x,z)$ (*e*,*f*) energy dissipation rates for $Pr=0.7$ (*c*,*e*) and 5.3 (*d*,*f*).

Figure 1(*c*–*f*) respectively displays the corresponding logarithmic fields of kinetic $\log_{10}\varepsilon_u$ and thermal $\log_{10}\varepsilon_\theta$ dissipation rates, where the local dissipation rate is indicated according to the colour bar. It is seen that the intense dissipations of both ε_u and ε_θ occur nearly in the regions with higher or lower temperature, which correspond to hot or cold plumes detaching from the thermal BLs. This suggests that

https://doi.org/10.1017/jfm.2017.19 Published online by Cambridge University Press

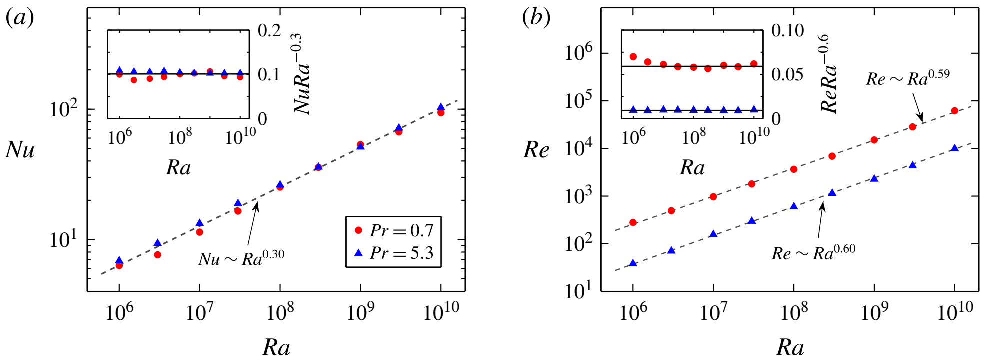

FIGURE 2. (Colour online) Log–log plots of Nu (*a*) and Re (*b*) as functions of Ra for $Pr = 0.7$ (circles) and 5.3 (triangles). The dashed lines are the best power-law fits to the corresponding data. The insets show the compensated plots $NuRa^{-0.3}$ versus Ra and $ReRa^{-0.6}$ versus Ra.

the rising and falling thermal plumes are associated with large amplitudes of both kinetic and thermal dissipation rates (Kerr 1996; Shishkina & Wagner 2007; Emran & Schumacher 2008). This also suggests a strong positive correlation between the two dissipation fields. Indeed, our calculation shows that the correlation coefficient between ε_u and ε_θ is larger than 0.4 for all the simulations, similar to the findings in 2-D Rayleigh–Taylor turbulence by Zhou & Jiang (2016).

We now come to the scaling relations of the Nusselt number Nu and the Reynolds number Re versus the Rayleigh number Ra. In the present study, Nu was calculated over the whole cell and over time via the definition (Verzicco & Camussi 2003; Verzicco & Sreenivasan 2008)

$$Nu = 1 + \sqrt{PrRa}\langle w\theta\rangle_{V,t}. \tag{3.1}$$

Due to the zero value for the velocity average over the whole cell, we here choose the root-mean-square (r.m.s.) velocity to define the Reynolds number (Sugiyama *et al.* 2009), i.e.

$$Re = \frac{U_{rms}H}{\nu}, \tag{3.2}$$

where $U_{rms} = \sqrt{\langle(u^2 + w^2)\rangle_{V,t}}$ can be used as a global measure for the strength of the convection. The convergence of both Nu and Re has been checked by comparing the time averages over the first and the last halves of each simulation, and the resulting relative error was smaller than 1 % for all of our simulations.

Figure 2(*a*) shows a log–log plot of the measured Nu as a function of Ra for the two Prandtl numbers $Pr = 0.7$ (circles) and 5.3 (triangles). The data can be well described by a power-law relation and the best fit gives $Nu = 0.099Ra^{-0.30\pm0.02}$, shown as the dashed line in the figure. We note that the present scaling agrees well with the previous numerical results found also in 2-D convection cells (Johnston & Doering 2009; van der Poel, Stevens, Sugiyama & Lohse 2012). We further note that the exponent 0.30 ± 0.02 is in general consistent with those obtained in 3-D cylindrical RB systems (Ahlers *et al.* 2009; Chillà & Schumacher 2012). This suggests that the heat transport in both 2-D and 3-D convection might be dominated by the same physical mechanism, and thus they could be modelled in a similar way. Indeed, as we shall see in § 3.3, the results obtained in the present 2-D settings obey the GL

https://doi.org/10.1017/jfm.2017.19 Published online by Cambridge University Press

phase diagram obtained for 3-D convection. Nevertheless, the prefactor 0.099 in the best fit relation is smaller than its counterpart for the 3-D cases where it varies between 0.12 and 0.15 (see, e.g. figure 2 of Wagner, Shishkina & Wagner (2012)). The possible reason is that in a closed system the convective flow would sometimes make hot (cold) plumes move downwards (upwards) and thus lead to strong count gradient/negative local heat flux (Huang & Zhou 2013), which impedes the overall heat transfer. This happens much more in two dimensions than in three dimensions.

Figure 2(*b*) displays the measured *Re* as a function of *Ra* in a log–log plot. Due to the decreasing viscosity ν, the Reynolds number for $Pr = 0.7$ is found to be much larger than that for $Pr = 5.3$. The best power-law fit to the data yields $Re \sim Ra^{0.59\pm0.02}$ for $Pr = 0.7$ and $Re \sim Ra^{0.60\pm0.01}$ for $Pr = 5.3$. The fitted scaling exponents are in excellent agreement with the exponent 0.62 found for 2-D Boussinesq RB convection by Sugiyama *et al.* (2009), but are notably larger than those varying from 0.42 to 0.5 seen for 3-D RB flows in various convecting fluids with wide parameter range and based on the single- or multi-point measurements. (Ashkenazi & Steinberg 1999; Niemela *et al.* 2001; Qiu & Tong 2001; Lam *et al.* 2002; Sun & Xia 2005; Brown, Funfschilling & Ahlers 2007). The difference in *Re* scaling is not captured by the GL model and implies that the convective flow in two dimensions has a stronger strength than in three dimensions. Indeed, direct comparison between 2-D and 3-D convection revealed a higher absolute value of the Reynolds number in two dimensions (van der Poel, Stevens & Lohse 2013). The possible reason is that in the 2-D geometry almost all plumes emitted from the top and bottom thermal BLs follow the motion of the large-scale convective rolls (including the corner-flow rolls), and then drive these large-scale rolls, due to the absence of the fluid motion in the third dimension, whereas this is not the case for three dimensions (van der Poel *et al.* 2013).

3.2. *Probability density functions (PDFs) of ε_u and ε_θ*

Next, we investigate the statistics of the kinetic ε_u and thermal ε_θ energy dissipation rates in this section. Figures 3(*a*,*b*) show the PDFs of ε_u obtained at $Pr = 0.7$ and 5.3, respectively. The corresponding PDFs of ε_θ are shown in figures 4(*a*,*b*). All data have been normalized with respect to their root-mean-square (r.m.s.) values $(\varepsilon_u)_{rms} = \sqrt{\langle \varepsilon_u^2 \rangle_{V,t}}$ and $(\varepsilon_\theta)_{rms} = \sqrt{\langle \varepsilon_\theta^2 \rangle_{V,t}}$. In the figures, two features are worthy of note. First, for both ε_u and ε_θ, the PDF tails become more extended with increasing *Ra* (and thus with increasing *Re*), implying an increasing degree of small-scale intermittency possessed by the both dissipation fields. This is in spite of the fact that the intermittency effects are expected to be absent for the velocity field in 2-D turbulent convection, as shown by Celani *et al.* (2002). It should be noted that the convective flow studied by Celani *et al.* (2002) is forced by a mean gradient, which has different boundary conditions from the present RB setting. Whether the intermittency in the statistics of velocity fluctuations is absent also in the present system needs to be verified, which requires a detailed study on the high-order moments of velocity increments. Second, at a given Rayleigh number, the PDFs of both ε_u and ε_θ obtained at lower Prandtl number ($Pr = 0.7$) have a fatter tail than those obtained at higher Prandtl number ($Pr = 5.3$). The reason for this might be attributed to the increasing *Re* (and thus an increasing degree of intermittency) with decreasing *Pr*, as shown in figure 2(*b*). This is in line with the observations in 3-D cylindrical RB systems (He *et al.* 2007; Emran & Schumacher 2008), but is different from the results observed by Schumacher & Sreenivasan (2005) for the passive scalar case, where the decreasing diffusivity with increasing *Pr* causes sharper gradients of the scalar field and hence generates fatter PDF tails.

https://doi.org/10.1017/jfm.2017.19 Published online by Cambridge University Press

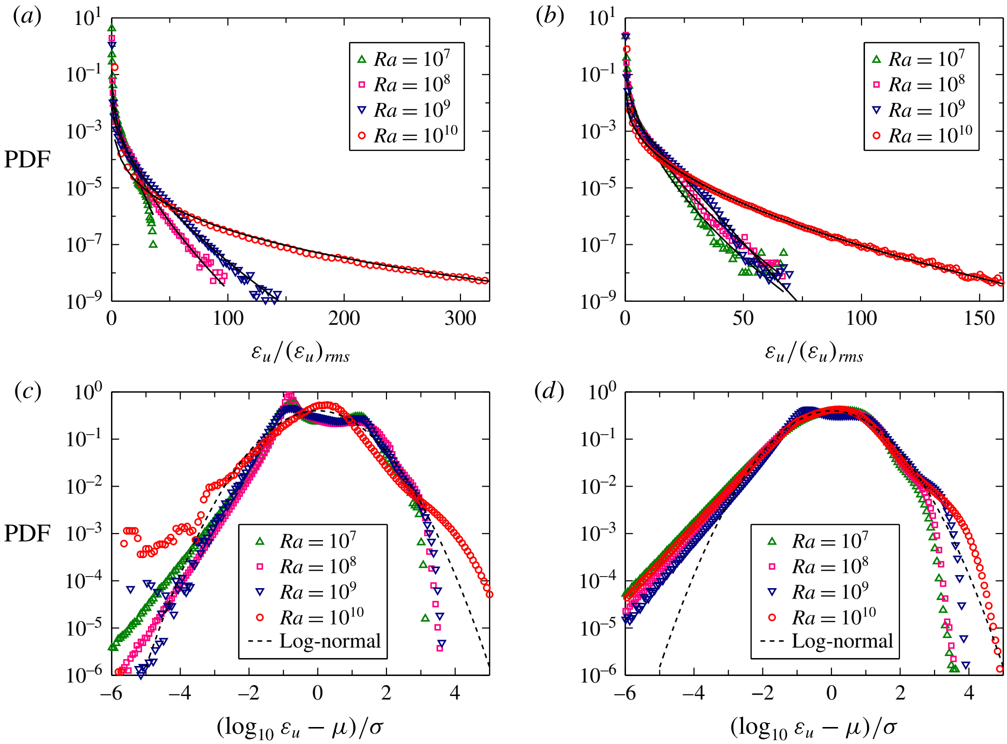

FIGURE 3. (Colour online) (a,b) PDFs of the kinetic energy dissipation rates, ε_u, obtained over the whole cell and normalized with respect to their r.m.s. values $(\varepsilon_u)_{rms}$. The solid lines are the best fits of stretched exponentials, as given by (3.3), to the corresponding tails. (c,d) PDFs of $\log_{10}\varepsilon_u$ calculated over the whole cell. Here, μ and σ are, respectively, the mean value and standard deviation of $\log_{10}\varepsilon_u$. The dashed lines mark the log-normal distribution for comparison. The data are obtained at $Pr = 0.7$ (a,c) and 5.3 (b,d).

To quantitatively describe the shape of the measured PDF tails, we note that a stretched exponential function, i.e.

$$p(Y) = \frac{C}{\sqrt{Y}}\exp(-mY^{\alpha}), \tag{3.3}$$

was derived analytically for the tails of passive scalar dissipation in the limit of large Peclet and Prandtl numbers in two dimensions and $\alpha = 1/3$ was found (Chertkov, Falkovich & Kolokolov 1998). This result was then extended to arbitrary space dimensions (Gamba & Kolokolov 1999), as the behaviour (3.3) is determined by the dynamics of stretching (not of rotation) that is likely to take place in any dimension (Chertkov *et al.* 1998). Here, C, m and α are fitting parameters, and $Y = X - X_{mp}$ with $X = \varepsilon_\theta/(\varepsilon_\theta)_{rms}$ and X_{mp} being the abscissa of the most probable (mp) amplitude. In numerical studies of passive scalar in turbulence, the function (3.3) was found to well fit to the fraction of the dissipation PDF that extends from the mp amplitude to the end of the tail (Overholt & Pope 1996; Schumacher & Sreenivasan 2005). The similar analysis was later conducted for active scalar in 3-D RB convection (Emran & Schumacher 2008; Kaczorowski & Wagner 2009) and in 2-D Rayleigh–Taylor turbulence (Zhou & Jiang 2016). Here, to follow this idea, we also adopted (3.3) to

https://doi.org/10.1017/jfm.2017.19 Published online by Cambridge University Press

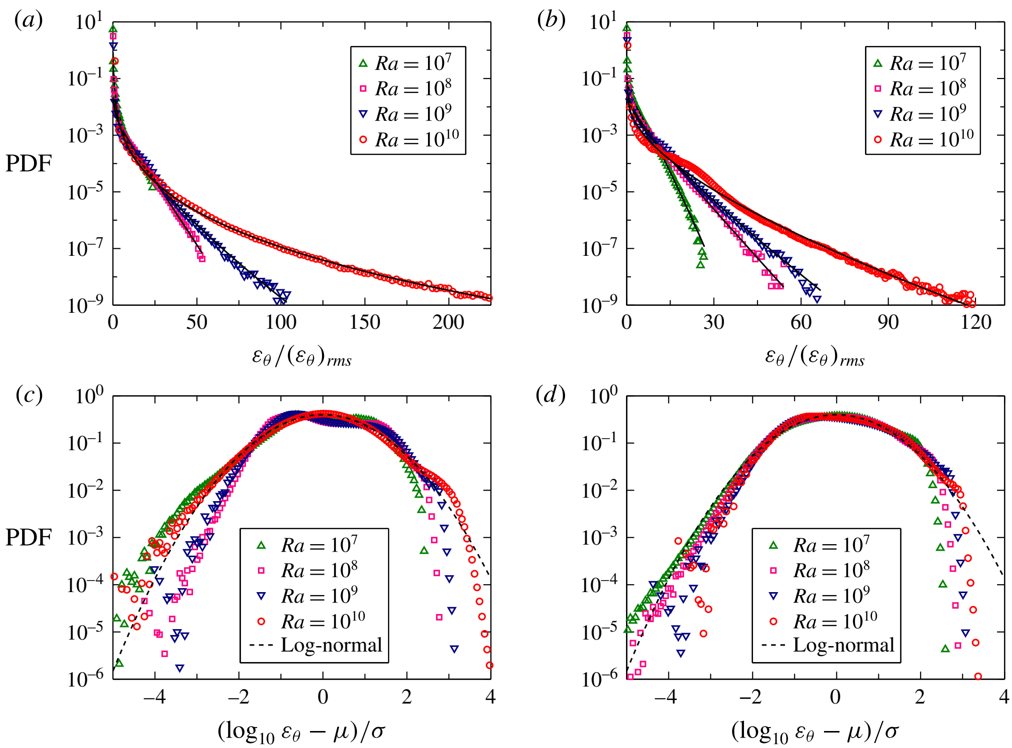

FIGURE 4. (Colour online) (*a*,*b*) PDFs of the thermal energy dissipation rates, ε_θ, obtained over the whole cell and normalized with respect to their r.m.s. values $(\varepsilon_\theta)_{rms}$. The solid lines are the best fits of stretched exponentials, as given by (3.3), to the corresponding tails. (*c*,*d*) PDFs of $\log_{10}\varepsilon_\theta$ calculated over the whole cell. Here, μ and σ are, respectively, the mean value and standard deviation of $\log_{10}\varepsilon_\theta$. The dashed lines mark the log-normal distribution for comparison. The data are obtained at $Pr = 0.7$ (*a*,*c*) and 5.3 (*b*,*d*).

fit the PDF tails for both ε_u and ε_θ obtained over the whole cell, and our results show that (3.3) can be indeed used to describe well the tails of the dissipation PDFs (see the solid lines in figures 3 and 4).

In some classical turbulence theories, like the refined similarity hypothesis proposed by Kolmogorov (1962), the dissipation fields are often assumed to have a log-normal distribution. However, the highly intermittent nature of the local dissipation generates the observed deviations from the log-normality (Ferchichi & Tavoularis 2002; Schumacher & Sreenivasan 2005; Emran & Schumacher 2008; Kaczorowski & Wagner 2009). To check the deviations in our present systems, the dissipation PDFs are represented in log-normal coordinates in figures 3(*c*,*d*) and 4(*c*,*d*). In the figures, the dashed lines mark the log-normal distribution for reference. Clear departures from log-normality can be seen for both ε_u and ε_θ. As *Ra* increases, the cores of the PDFs seem to converge towards the log-normality and the right tails become fatter, while the left tails do not appear to show systematic trends with the Rayleigh number.

3.3. *Spatial distribution of ε_u and ε_θ*

Figure 5(*a*–*d*) show the vertical profiles of $\langle\varepsilon_u\rangle_{x,t}$ and $\langle\varepsilon_\theta\rangle_{x,t}$, which illustrate the spatial distribution of the dissipation rates. Here, $\langle\cdot\rangle_{x,t}$ denotes an average over the horizontal direction and over time. The kinetic energy dissipation rate keeps nearly

https://doi.org/10.1017/jfm.2017.19 Published online by Cambridge University Press

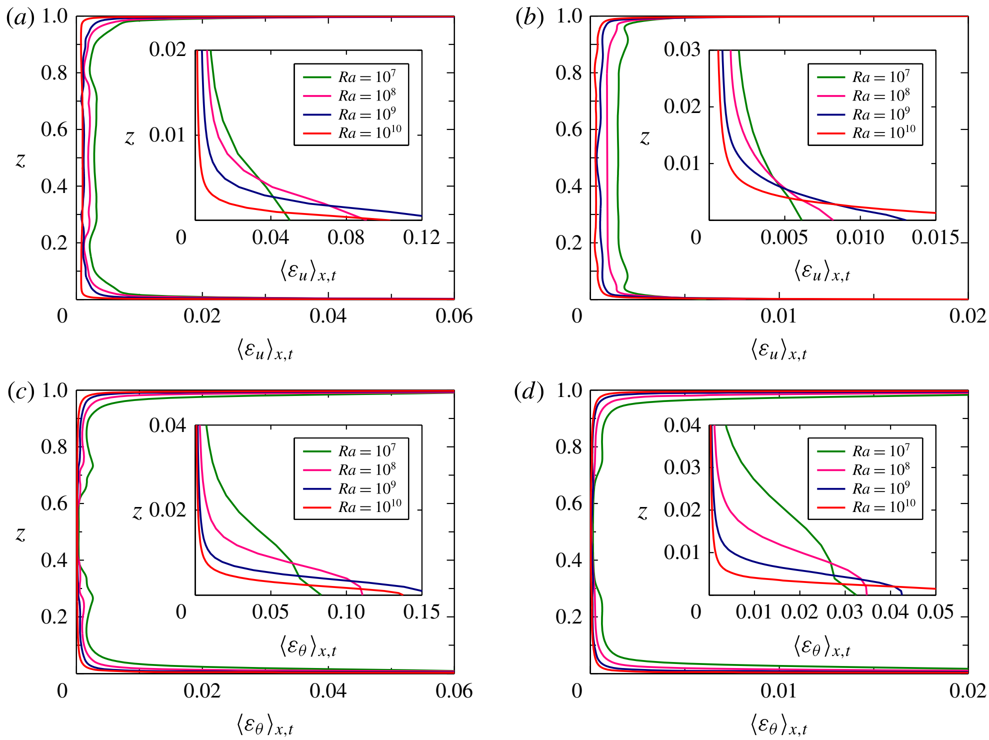

FIGURE 5. (Colour online) Averaged vertical profiles of kinetic (*a*,*b*) and thermal (*c*,*d*) energy dissipation rates obtained at $Pr = 0.7$ (*a*,*c*) and 5.3 (*b*,*d*). The insets show an enlarged portion of the profiles close to the bottom plate.

constant in the bulk, increases rapidly in the neighbourhood of the top and bottom plates where viscosity becomes significant, and reaches its maximum value at the solid-fluid interfaces. With decreasing Ra, the magnitude of $\langle \varepsilon_u \rangle_{x,t}$ enhances in the bulk, but drops in the BL, indicating that the kinetic energy is dissipated more equally over the whole cell at lower Rayleigh numbers. The thermal dissipation rate also attains its largest value near the plates. However, in the core region ($0.4 \lesssim z \lesssim 0.6$) $\langle \varepsilon_\theta \rangle_{x,t}$ has almost a zero value for all data, suggesting that most thermal energy is dissipated within the thermal BLs.

To further quantify the spatial distribution, we calculate the dissipation contributions coming from the bulk region, separated from those coming from the BLs, i.e.

$$\langle \varepsilon_u \rangle_{V,t} = \langle \varepsilon_u \rangle_{V_{BL},t} + \langle \varepsilon_u \rangle_{V_{bulk},t}, \tag{3.4}$$

and

$$\langle \varepsilon_\theta \rangle_{V,t} = \langle \varepsilon_\theta \rangle_{V_{BL},t} + \langle \varepsilon_\theta \rangle_{V_{bulk},t}, \tag{3.5}$$

where V_{BL} and V_{bulk} denote the BL and bulk regions, respectively, and the averages $\langle \cdot \rangle_{V_{BL},t}$ and $\langle \cdot \rangle_{V_{bulk},t}$ have been multiplied by their corresponding volume percentages. Note that the splitting (3.4) and (3.5) are the central idea of the GL theory (Ahlers *et al.* 2009). To do this splitting, the BL thickness must be first defined to separate the bulk and BL regions. There are quite a few definitions of BL thickness, based on either the mean velocity/temperature profiles or their r.m.s. profiles (Sun *et al.* 2005;

https://doi.org/10.1017/jfm.2017.19 Published online by Cambridge University Press

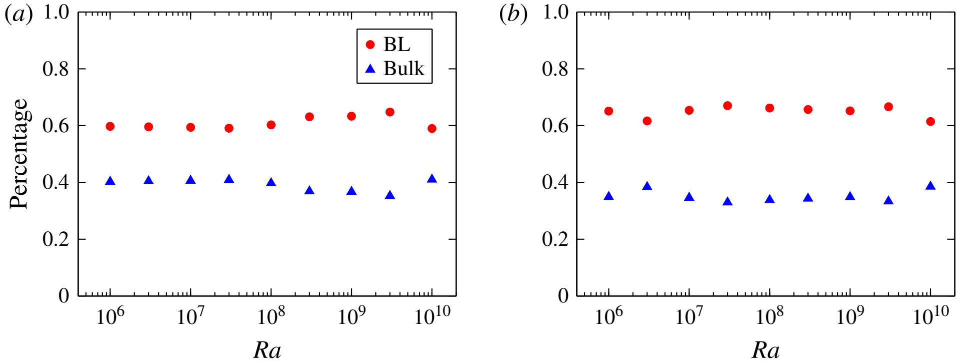

FIGURE 6. (Colour online) Percentages of bulk (triangles) and BL (circles) contributions to the kinetic energy dissipation rates, ε_u, as functions of Ra at $Pr=0.7$ (*a*) and 5.3 (*b*).

du Puits, Resagk & Thess 2010; Zhou & Xia 2010, 2013; Scheel, Kim & White 2012; Scheel & Schumacher 2014; Ng *et al.* 2015; Shishkina *et al.* 2015). In 2-D RB convection, however, due to the influences of the corner-flow rolls, the mean velocity profiles might sometimes lead to unphysical viscous BL thickness, as shown by Zhou *et al.* (2011). Therefore, in the present study, we define the viscous (thermal) BL thickness, δ_u^{rms} (δ_θ^{rms}), as the distance between the wall and the position at which the r.m.s. velocity (temperature) is maximum. We find that this definition gives a thermal BL thickness, δ_θ^{rms}, that is very close to the global estimation $H/(2Nu)$. We further find that whereas δ_u^{rms} increases with increasing Pr, δ_θ^{rms} at each Ra keeps nearly unchanged for both Pr. The ratio between δ_u^{rms} and δ_θ^{rms} varies around 0.85 for $Pr=0.7$, but between 1.5 and 4 for $Pr=5.3$. This is qualitatively consistent with the findings in 3-D cylindrical cells by Stevens, Lohse & Verzicco (2011).

As no-slip velocity boundary conditions are applied to all the solid surfaces, the velocity field has BLs close to both the two horizontal conducting plates and the two vertical side walls, whose thicknesses are determined from the horizontal and vertical r.m.s. velocity profiles, respectively. On the other hand, due to the adiabatic side walls, the thermal BLs include only those coming from the two horizontal plates. This BL–bulk partition is consistent with the distinction proposed by the GL theory (see figure 2 of Ahlers *et al.* 2009) and has been adopted in previous studies (Verzicco 2003; Verzicco & Camussi 2003).

The relative contributions of the bulk and BL regions to the total $\langle\varepsilon_u\rangle_{V,t}$ and $\langle\varepsilon_\theta\rangle_{V,t}$ are plotted as functions of Ra in figures 6 and 7. It is seen that for our present parameter ranges both ε_u and ε_θ are dominated by the BLs. Despite figures 5(*a*,*b*) reveal that at lower Rayleigh numbers the kinetic energy is dissipated more equally over the whole cell, the contribution to ε_u from the BL regions is still dominant as the BL thicknesses (and thus the volume fraction occupied by the BLs) increases with decreasing Ra. According to these results, the present series of simulations at $Pr=0.7$ and 5.3 can be classified as I_l and I_u regimes in the GL theory, respectively. Indeed, when placing the Ra and Pr values of the present simulations into the phase diagram of the GL theory (see figure 2 of Grossmann & Lohse 2000), we observe reasonable agreement. Nevertheless, it should be noted that the GL phase diagram (Grossmann & Lohse 2000) is obtained for 3-D convection, while the present simulations are performed in two dimensions. Previous studies on the comparison between 2-D and 3-D RB convection (van der Poel *et al.* 2013) have revealed that the *Nu*–*Ra* scaling

https://doi.org/10.1017/jfm.2017.19 Published online by Cambridge University Press

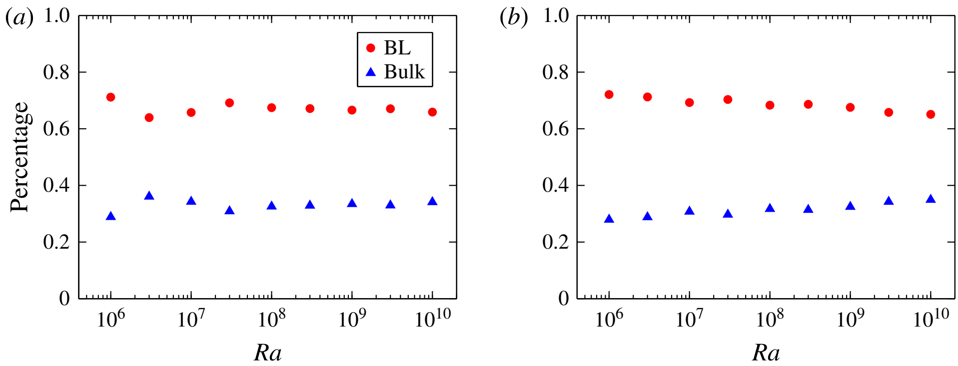

FIGURE 7. (Colour online) Percentages of bulk (triangles) and BL (circles) contributions to the thermal energy dissipation rates, ε_θ, as functions of Ra at $Pr=0.7$ (*a*) and 5.3 (*b*).

for 2-D and 3-D cases is very similar at higher Pr, differing only by a constant factor, while the difference is large at lower Pr, due to the strong roll state dependence of Nu in 2-D convection.

As the BL–bulk partition ignores the effects of thermal plumes which should be included in the BL estimates, Grossmann & Lohse (2004) suggested to use the labels pl (plume) and bg (background) for the two parts of the thermal energy dissipation rates, i.e.

$$\langle \varepsilon_\theta \rangle_{V,t} = \langle \varepsilon_\theta \rangle_{V_{pl},t} + \langle \varepsilon_\theta \rangle_{V_{bg},t}. \tag{3.6}$$

Here, $\langle \varepsilon_\theta \rangle_{V_{pl},t}$ indicates the contributions from the plumes together with the BL and $\langle \varepsilon_\theta \rangle_{V_{bg},t}$ signals those from the background. This pl–bg partition has been adopted in some previous numerical studies to investigate the distribution of ε_θ in 3-D cylindrical cells (Shishkina & Wagner 2006; Emran & Schumacher 2012). Next, we also consider the pl–bg partition. To detect thermal plumes, we follow the approach of Huang *et al.* (2013) and van der Poel, Verzicco, Grossmann & Lohse (2015). A thermal plume in the bulk is defined as a region where

$$|\theta(x, z, t) - \langle \theta \rangle_{x,t}| > c\theta_{rms} \quad \text{and} \quad \sqrt{PrRa}|w(x, z, t)\theta(x, z, t)| > cNu. \tag{3.7a,b}$$

Here, we consider the absolute value of the local convective heat flux, $|w(x, z, t)\, \theta(x, z, t)|$, because thermal plumes may sometimes generate negative local heat transport, which happens much more in two dimensions than in three dimensions, as revealed by Huang & Zhou (2013). The empirical constant c is chosen to be 1.2, which is the same as that of van der Poel *et al.* (2015) but larger than the value of 0.8 chosen by Huang *et al.* (2013). In a previous work in 3-D convection, Emran & Schumacher (2012) identified thermal plumes by using a similar threshold that is based only on $w\theta$ and they found that the increase of the threshold by two orders of magnitude causes slight variations in the Ra scaling. In the present work, we also find that the Re scalings of $\langle \varepsilon_\theta \rangle_{V_{pl},t}$ and $\langle \varepsilon_\theta \rangle_{V_{bg},t}$ do not depend apparently on the value of threshold c. Figure 8(*b*) depicts the V_{pl} regions (in black) by applying the criterion (3.7*a*,*b*) to the instantaneous temperature snapshot shown in figure 8(*a*).

Figures 9(*a*,*b*) shows the relative contributions from V_{pl} and V_{bg} to the total $\langle \varepsilon_\theta \rangle_{V,t}$, as functions of Ra. Clearly, ε_θ is plume dominated for the present parameter ranges. When varying the value of threshold c, a systematic trend can be observed for both

https://doi.org/10.1017/jfm.2017.19 Published online by Cambridge University Press

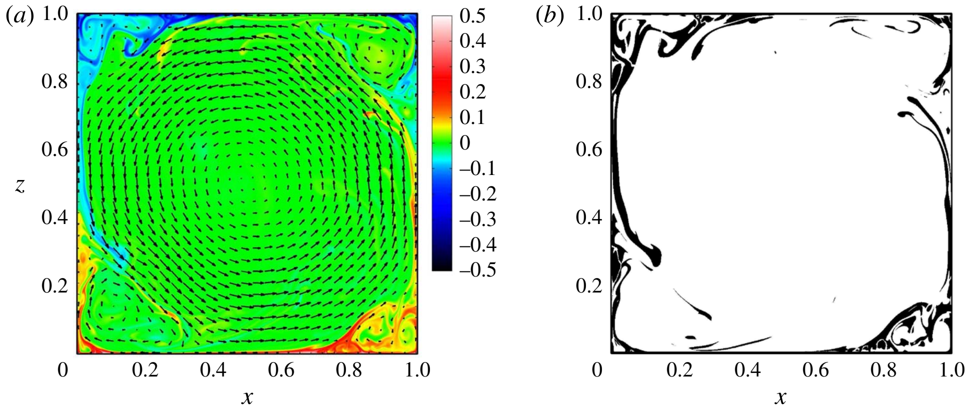

FIGURE 8. (*a*) A snapshot of the instantaneous temperature (colour) and velocity (arrows) fields for $Ra = 10^{10}$ and $Pr = 5.3$. (*b*) The plume regions for the same snapshot are marked in black, otherwise white.

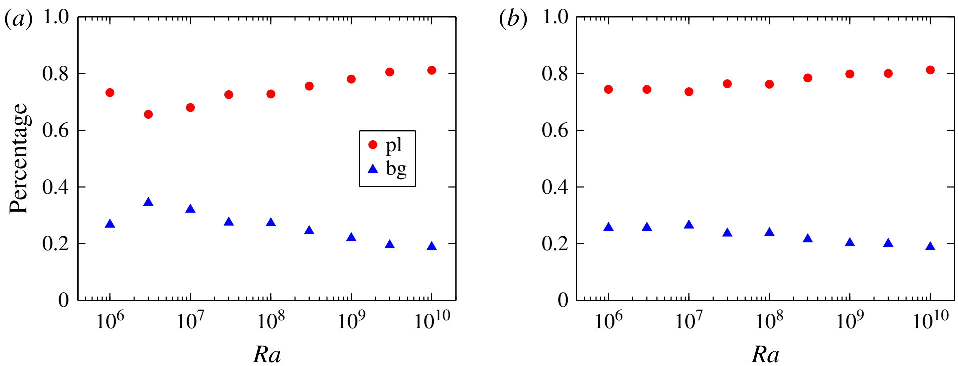

FIGURE 9. Percentages of plume (triangles) and background (circles) contributions to the thermal energy dissipation rates, ε_θ, as functions of *Ra* at $Pr = 0.7$ (*a*) and 5.3 (*b*).

contributions. The smaller the threshold c, the more the V_{pl} contribution data are shifted upwards and those from V_{bg} downwards. Moreover, when the threshold c becomes large enough, the V_{pl} region will become negligibly small and then the pl–bg partition will be the same as the BL–bulk partition.

3.4. *Ra and Re dependence*

Finally, we consider the *Ra* and *Re* dependence of the dissipation rates. Figure 10(*a*,*b*) show the total dissipation rates, $\langle\varepsilon_u\rangle_{V,t}$ and $\langle\varepsilon_\theta\rangle_{V,t}$, as functions of *Ra* in log–log plots. The solid lines in the figure represent the best power-law fits to the corresponding data, which yield

$$\langle\varepsilon_u\rangle_{V,t} = 0.077Ra^{-0.18\pm0.02} \quad \text{and} \quad \langle\varepsilon_\theta\rangle_{V,t} = 0.10Ra^{-0.19\pm0.02} \quad \text{for } Pr = 0.7, \qquad (3.8a,b)$$

$$\langle\varepsilon_u\rangle_{V,t} = 0.036Ra^{-0.19\pm0.01} \quad \text{and} \quad \langle\varepsilon_\theta\rangle_{V,t} = 0.050Ra^{-0.20\pm0.01} \quad \text{for } Pr = 5.3. \qquad (3.9a,b)$$

One sees that $\langle\varepsilon_u\rangle_{V,t}$ and $\langle\varepsilon_\theta\rangle_{V,t}$ have similar scaling behaviours with *Ra* but their magnitudes vary with *Pr*.

https://doi.org/10.1017/jfm.2017.19 Published online by Cambridge University Press

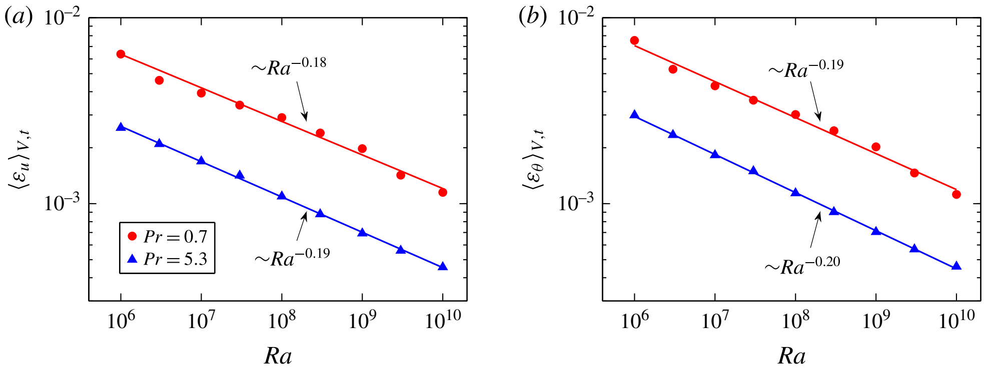

FIGURE 10. (Colour online) The Ra dependence of $\langle\varepsilon_u\rangle_{V,t}$ (a) and $\langle\varepsilon_\theta\rangle_{V,t}$ (b) calculated at $Pr = 0.7$ (circles) and 5.3 (triangles). The solid lines represent the best power-law fits to the corresponding data.

To understand these scaling behaviours, we note that figure 2(a) has shown that $Nu \sim Ra^{0.3}$. Plug it into the two global exact relations (1.5) and (1.6), we have

$$\langle\varepsilon_u\rangle_{V,t} = (Nu-1)/\sqrt{RaPr} \sim Ra^{-0.2} \quad \text{and} \quad \langle\varepsilon_\theta\rangle_{V,t} = Nu/\sqrt{RaPr} \sim Ra^{-0.2}. \quad (3.10a,b)$$

Comparing (3.10a,b) to our measured scalings (3.8a,b) and (3.9a,b) in figure 10, one observes very good agreement within numerical uncertainty, again verifying that the global exact relations for $\langle\varepsilon_u\rangle_{V,t}$ and $\langle\varepsilon_\theta\rangle_{V,t}$ are satisfied for our present simulations.

The essence of the GL theory (Grossmann & Lohse 2000) is the splitting of the total dissipation rates into the contributions from the bulk and BL regions, i.e. the relations (3.4) and (3.5). By assuming that there exist a large-scale mean flow (associated with a Reynolds number Re) in the system and that the BLs are characterized by a single effective thickness, the four contributions to the dissipation can be estimated as follows:

$$\langle\varepsilon_u\rangle_{V_{BL},t} \sim \frac{\nu^3}{H^4} Re^{5/2}, \quad (3.11)$$

$$\langle\varepsilon_u\rangle_{V_{bulk},t} \sim \frac{\nu^3}{H^4} Re^{3}, \quad (3.12)$$

$$\langle\varepsilon_\theta\rangle_{V_{BL},t} \sim \kappa\frac{\Delta^2}{H^2} Re^{1/2} g(Pr), \quad (3.13)$$

$$\langle\varepsilon_\theta\rangle_{V_{bulk},t} \sim \kappa\frac{\Delta^2}{H^2} PrRe, \quad (3.14)$$

where $g(Pr)$ is a function of Pr. When the plume effects are included in the BL estimates, we have

$$\langle\varepsilon_\theta\rangle_{V_{pl},t} \sim \kappa\frac{\Delta^2}{H^2} Re^{1/2} Pr^{1/2} f^{1/2}, \quad (3.15)$$

$$\langle\varepsilon_\theta\rangle_{V_{bg},t} \sim \kappa\frac{\Delta^2}{H^2} RePrf, \quad (3.16)$$

where, f is a shedding frequency that has no systematic dependence on Reynolds number. To test these scalings, we examine the Re dependence of the normalized

https://doi.org/10.1017/jfm.2017.19 Published online by Cambridge University Press

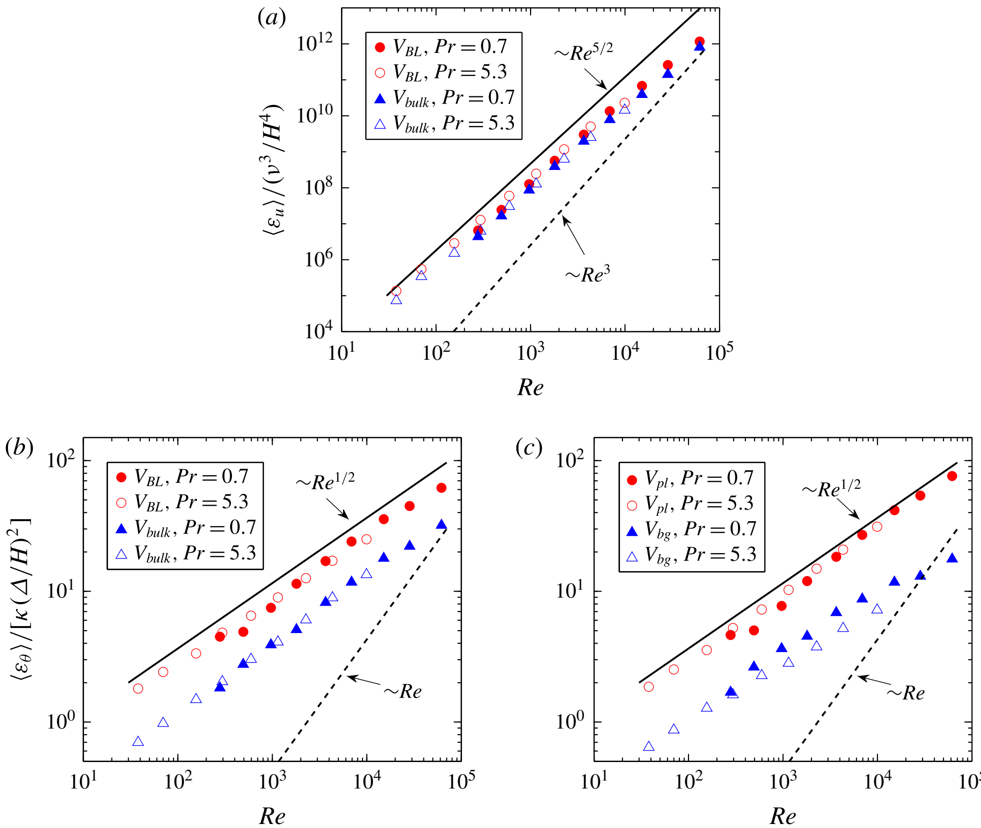

FIGURE 11. (Colour online) (*a*,*b*) The *Re* dependence of the normalized dissipation in the bulk and BL regions for $\langle \varepsilon_u \rangle/(\nu^3/H^4)$ (*a*) and $\langle \varepsilon_\theta \rangle/[\kappa(\Delta/H)^2]$ (*b*) obtained at $Pr = 0.7$ and 5.3. For reference, the solid and dashed lines mark the GL predictions (3.11)–(3.14), respectively, for the BL and bulk contributions. (*c*) The *Re* dependence of the normalized thermal energy dissipation rates in the plume and background regions. For reference, the solid and dashed lines mark the GL predictions (3.15)–(3.16), respectively, for the plume and background contributions.

dissipations in figure 11. Figure 11(*a*,*b*) shows the results from the BL–bulk partition. It is seen that both the BL and bulk contributions exhibit parallel trends as *Re* increases. This is consistent with the observations in figures 6 and 7, which show that the ratio of the BL-to-bulk contributions for both $\langle \varepsilon_u \rangle$ and $\langle \varepsilon_\theta \rangle$ appears to be constant. Figure 11(*c*) shows the results from the pl–bg partition for ε_θ. Similar to the BL–bulk partition, the contributions from V_{pl} and V_{bg} also exhibit roughly parallel trends with increasing *Re*. We further find that these trends and their *Re* scaling do not change apparently with the value of threshold *c*.

In addition, while the BL/plume contributions, $\langle \varepsilon_u \rangle_{V_{BL},t}$, $\langle \varepsilon_\theta \rangle_{V_{BL},t}$, and $\langle \varepsilon_\theta \rangle_{V_{pl},t}$, follow well the GL predictions (3.11), (3.13), and (3.15) (the solid lines in figure 11), the bulk/background contributions, $\langle \varepsilon_u \rangle_{V_{bulk},t}$, $\langle \varepsilon_\theta \rangle_{V_{bulk},t}$, and $\langle \varepsilon_\theta \rangle_{V_{bg},t}$ deviate obviously from the predicted *Re* scalings (3.12), (3.14) and (3.16) (the dashed lines in figure 11). Similar deviations for the bulk contributions have already been reported in homogeneous convection (Calzavarini *et al.* 2005), turbulent RB convection in

https://doi.org/10.1017/jfm.2017.19 Published online by Cambridge University Press

spherical shells (Gastine, Wicht & Aurnou 2015) and vertical natural convection (Ng *et al.* 2015). In the present study, the reason for the deviation of $\langle\varepsilon_u\rangle_{V_{bulk},t}$ from (3.12) is that the GL scaling (3.12) for the bulk contributions is based on the Kolmogorov's picture in which the kinetic energy cascades from large to small scales. This assumption, however, does not hold in 2-D RB convection, where an inverse cascade of kinetic energy from small to large scales is theoretically expected (Celani *et al.* 2002). Indeed, the calculation of the third-order structure function of longitudinal velocity increments, $S_3(r) = \langle(w(r+z) - w(z))^3\rangle_{V,t}$, shows that $S_3(r)$ is positive over all scales studied (not shown here), signalling the reversal of the kinetic energy cascade in the present 2-D RB setting. A detailed study on this issue is out of the scope of the present work.

4. Conclusion

In this paper, we present an analysis of the statistical properties of the kinetic and thermal energy dissipation rates in 2-D turbulent RB convection, by means of high-resolution DNS, with Pr fixed at 0.7 and 5.3 and Ra varying from 10^6 to 10^{10}. Major findings are summarized as follows:

(i) The global heat transport and momentum scaling exponents are examined, which yields $Nu \sim Ra^{0.30\pm0.02}$ and $Re \sim Ra^{0.60\pm0.02}$ for both Pr. When comparing with previous numerical and experimental results obtained in the 3-D cases, $Nu(Ra)$ is found to have a similar scaling exponent with smaller amplitudes, suggesting that the heat transport in both 2-D and 3-D convection might be dominated by the same physical mechanism and thus could be modelled in a similar way. Whereas the exponent of $Re(Ra)$ is notably larger than its 3-D counterpart, implying a stronger strength of the convective flow in two dimensions than in three dimensions.

(ii) Similar to the 3-D situations, the PDFs of both ε_u and ε_θ in 2-D RB convection are found to be always non-log-normal, but their tails can be well fitted by a stretched exponential function. These tails become more extended with increasing Ra or decreasing Pr, which displays an increasing degree of small-scale intermittency with increasing Re. This is in spite of that intermittency is expected to be absent for velocity in 2-D turbulent convection (Celani *et al.* 2002). The ensemble averages of both dissipation rates scale as $Ra^{-0.18\sim-0.20}$. This scaling exponent agrees well with those estimated from the two global exact relations (1.5) and (1.6).

(iii) When considering the dissipation contributions that come from the bulk and BL regions, we find that $\langle\varepsilon_u\rangle_{V,t}$ and $\langle\varepsilon_\theta\rangle_{V,t}$ are both dominated by the BLs. This corresponds to regimes I_l and I_u in the GL theory (Grossmann & Lohse 2000) for our present simulations of $Pr = 0.7$ and 5.3 respectively. To include the effects of thermal plumes, the pl–bg partition is also considered and $\langle\varepsilon_\theta\rangle_{V,t}$ is found to be plume dominated. Further analysis reveals that the BL/pl contributions scale as those predicted by the GL theory, while the deviations from the GL predictions are observed for the bulk/bg contributions.

Acknowledgements

This work was supported by Natural Science Foundation of China under grant nos 11672156, 11572185, and 11332006, Shanghai Shuguang Project under grant no. 13SG40 and Program for New Century Excellent Talents in University under

https://doi.org/10.1017/jfm.2017.19 Published online by Cambridge University Press

grant no. NCET-13. Q.Z. wishes to acknowledge support given to him from the organization department of the CPC central committee through the National Program for Support of Top-notch Young Professionals.

REFERENCES

AHLERS, G., GROSSMANN, S. & LOHSE, D. 2009 Heat transfer and large scale dynamics in turbulent Rayleigh–Bénard convection. *Rev. Mod. Phys.* **81**, 503–537.

ASHKENAZI, S. & STEINBERG, V. 1999 Spectra and statistics of velocity and temperature fluctuations in turbulent convection. *Phys. Rev. Lett.* **83**, 4760.

BROWN, E., FUNFSCHILLING, D. & AHLERS, G. 2007 Anomalous Reynolds-number scaling in turbulent Rayleigh–Bénard convection. *J. Stat. Mech.* **10**, P10005.

CALZAVARINI, E., LOHSE, D., TOSCHI, F. & TRIPICCIONE, R. 2005 Rayleigh and Prandtl number scaling in the bulk of Rayleigh–Bénard convection. *Phys. Fluids* **17**, 055107.

CELANI, A., MATSUMOTO, T., MAZZINO, A. & VERGASSOLA, M. 2002 Scaling and universality in turbulent convection. *Phys. Rev. Lett.* **88**, 054503.

CHANDRA, M. & VERMA, M. K. 2013 Flow reversals in turbulent convection via vortex reconnections. *Phys. Rev. Lett.* **110**, 114503.

CHERTKOV, M., FALKOVICH, G. & KOLOKOLOV, I. 1998 Intermittent dissipation of a passive scalar in turbulence. *Phys. Rev. Lett.* **80**, 2121–2124.

CHILLÀ, F. & SCHUMACHER, J. 2012 New perspectives in turbulent Rayleigh–Bénard convection. *Eur. Phys. J.* E **35**, 58.

EMRAN, M. S. & SCHUMACHER, J. 2008 Fine-scale statistics of temperature and its derivatives in convective turbulence. *J. Fluid Mech.* **611**, 13–34.

EMRAN, M. S. & SCHUMACHER, J. 2012 Conditional statistics of thermal dissipation rate in turbulent Rayleigh–Bénard convection. *Eur. Phys. J.* E **35**, 108.

FERCHICHI, M. & TAVOULARIS, S. 2002 Scalar probability density function and fine structure in uniformly sheared turbulence. *J. Fluid Mech.* **461**, 155–182.

GAMBA, A. & KOLOKOLOV, I. 1999 Dissipation statistics of a passive scalar in a multidimensional smooth flow. *J. Stat. Phys.* **94**, 759–777.

GASTINE, T., WICHT, J. & AURNOU, J. M. 2015 Turbulent Rayleigh–Bénard convection in spherical shells. *J. Fluid Mech.* **778**, 721–764.

GROSSMANN, S. & LOHSE, D. 2000 Scaling in thermal convection: a unifying theory. *J. Fluid Mech.* **407**, 27–56.

GROSSMANN, S. & LOHSE, D. 2004 Fluctuations in turbulent Rayleigh–Bénard convection: the role of plumes. *Phys. Fluids* **16**, 4462.

GRÖTZBACH, G. 1983 Spatial resolution requirements for direct numerical simulation of the Rayleigh–Bénard convection. *J. Comput. Phys.* **49**, 241–269.

HE, X.-Z., CHING, E. S. C. & TONG, P. 2011 Locally averaged thermal dissipation rate in turbulent thermal convection: a decomposition into contributions from different temperature gradient components. *Phys. Fluids* **23**, 025106.

HE, X.-Z. & TONG, P. 2009 Measurements of the thermal dissipation field in turbulent Rayleigh–Bénard convection. *Phys. Rev.* E **79**, 026306.

HE, X.-Z., TONG, P. & CHING, E. S. C. 2010 Statistics of the locally averaged thermal dissipation rate in turbulent Rayleigh–Bénard convection. *J. Turbul.* **11** (35), 1–10.

HE, X.-Z., TONG, P. & XIA, K.-Q. 2007 Measured thermal dissipation field in turbulent Rayleigh–Bénard convection. *Phys. Rev. Lett.* **98**, 144501.

HUANG, S.-D., KACZOROWSKI, M., NI, R. & XIA, K.-Q. 2013 Confinement-induced heat-transport enhancement in turbulent thermal convection. *Phys. Rev. Lett.* **111**, 104501.

HUANG, Y.-X. & ZHOU, Q. 2013 Counter-gradient heat transport in two-dimensional turbulent Rayleigh–Bénard convection. *J. Fluid Mech.* **737**, R3.

JOHNSTON, H. & DOERING, C. R. 2009 Comparison of temperature thermal convection between conditions of constant temperature and constant flux. *Phys. Rev. Lett.* **102**, 064501.

https://doi.org/10.1017/jfm.2017.19 Published online by Cambridge University Press

KACZOROWSKI, M. & WAGNER, C. 2009 Analysis of the thermal plumes in turbulent Rayleigh–Bénard convection based on well-resolved numerical simulations. *J. Fluid Mech.* **618**, 89–112.

KADANOFF, L. P. 2001 Turbulent heat flow: structures and scaling. *Phys. Today* **54** (8), 34–39.

KERR, R. 1996 Rayleigh number scaling in numerical convection. *J. Fluid Mech.* **310**, 139–179.

KOLMOGOROV, A. N. 1962 A refinement of previous hypotheses concerning the local structure of turbulence in a viscous incompressible fluid at high Reynolds number. *J. Fluid Mech.* **13**, 82–85.

LAM, S., SHANG, X.-D., ZHOU, S.-Q. & XIA, K.-Q. 2002 Prandtl number dependence of the viscous boundary layer and the Reynolds numbers in Rayleigh–Bénard convection. *Phys. Rev.* E **65**, 066306.

LIU, J.-G., WANG, C. & JOHNSTON, H. 2003 A fourth order scheme for incompressible Boussinesq equations. *J. Sci. Comput.* **18**, 253–285.

LOHSE, D. & XIA, K.-Q. 2010 Small-scale properties of turbulent Rayleigh–Bénard convection. *Annu. Rev. Fluid Mech.* **42**, 335–364.

NG, C. S., OOI, A., LOHSE, D. & CHUNG, D. 2015 Vertical natural convection: application of the unifying theory of thermal convection. *J. Fluid Mech.* **764**, 349–361.

NI, R., HUANG, S.-D. & XIA, K.-Q. 2011 Local energy dissipation rate balances local heat flux in the center of turbulent thermal convection. *Phys. Rev. Lett.* **107**, 174503.

NIEMELA, J. J., SKRBEK, L., SREENIVASAN, K. R. & DONNELLY, R. J. 2001 The wind in confined thermal convection. *J. Fluid Mech.* **449**, 169–178.

OVERHOLT, M. R. & POPE, S. B. 1996 Direct numerical simulation of a passive scalar with imposed mean gradient in isotropic turbulence. *Phys. Fluids* **8**, 3128–3148.

PETSCHEL, K., STELLMACH, S., WILCZEK, M., LÜLFF, J. & HANSEN, U. 2013 Dissipation layers in Rayleigh–Bénard convection: a unifying view. *Phys. Rev. Lett.* **110**, 114502.

PETSCHEL, K., STELLMACH, S., WILCZEK, M., LÜLFF, J. & HANSEN, U. 2015 Kinetic energy transport in Rayleigh–Bénard convection. *J. Fluid Mech.* **773**, 395–417.

VAN DER POEL, E. P., STEVENS, R. J. A. M. & LOHSE, D. 2013 Comparison between two- and three-dimensional Rayleigh–Bénard convection. *J. Fluid Mech.* **736**, 177–194.

VAN DER POEL, E. P., STEVENS, R. J. A. M., SUGIYAMA, K. & LOHSE, D. 2012 Flow states in two-dimensional Rayleigh–Bénard convection as a function of aspect-ratio and Rayleigh number. *Phys. Fluids* **24**, 085104.

VAN DER POEL, E. P., VERZICCO, R., GROSSMANN, S. & LOHSE, D. 2015 Plume emission statistics in turbulent Rayleigh–Bénard convection. *J. Fluid Mech.* **772**, 5–15.

DU PUITS, R., RESAGK, C. & THESS, A. 2007 Mean velocity profile in confined turbulent convection. *Phys. Rev. Lett.* **99**, 234504.

DU PUITS, R., RESAGK, C. & THESS, A. 2010 Measurements of the instantaneous local heat flux in turbulent Rayleigh–Bénard convection. *New J. Phys.* **12**, 075023.

QIU, X., LIU, Y.-L. & ZHOU, Q. 2014 Local dissipation scales in two-dimensional Rayleigh–Taylor turbulence. *Phys. Rev.* E **90**, 043012.

QIU, X.-L. & TONG, P. 2001 Large-scale velocity structures in turbulent thermal convection. *Phys. Rev. Lett.* **64**, 036304.

SCHEEL, J. D., KIM, E. & WHITE, K. R. 2012 Thermal and viscous boundary layers in turbulent Rayleigh–Bénard convection. *J. Fluid Mech.* **711**, 281–305.

SCHEEL, J. D. & SCHUMACHER, J. 2014 Local boundary layer scales in turbulent Rayleigh–Bénard convection. *J. Fluid Mech.* **758**, 344–373.

SCHUMACHER, J. & SREENIVASAN, K. R. 2005 Statistics and geometry of passive scalars in turbulence. *Phys. Fluids* **17**, 125107.

SHISHKINA, O., HORN, S., WAGNER, S. & CHING, E. S. C. 2015 Thermal boundary layer equation for turbulent Rayleigh–Bénard convection. *Phys. Rev. Lett.* **114**, 114302.

SHISHKINA, O., STEVENS, R. J. A. M., GROSSMANN, S. & LOHSE, D. 2010 Boundary layer structure in turbulent thermal convection and its consequences for the required numerical resolution. *New J. Phys.* **12**, 075022.

https://doi.org/10.1017/jfm.2017.19 Published online by Cambridge University Press

SHISHKINA, O. & WAGNER, C. 2006 Analysis of thermal dissipation rates in turbulent Rayleigh–Bénard convection. *J. Fluid Mech.* **546**, 51–60.

SHISHKINA, O. & WAGNER, C. 2007 Local heat fluxes in turbulent Rayleigh–Bénard convection. *Phys. Fluids* **19**, 085107.

SHISHKINA, O. & WAGNER, C. 2008 Analysis of sheet-like thermal plumes in turbulent Rayleigh–Bénard convection. *J. Fluid Mech.* **599**, 383–404.

SILANO, G., SREENIVASAN, K. R. & VERZICCO, R. 2010 Numerical simulations of Rayleigh–Bénard convection for Prandtl numbers between 10^{-1} and 10^4 and Rayleigh numbers between 10^5 and 10^9. *J. Fluid Mech.* **662**, 409–446.

STEVENS, R. J. A. M., LOHSE, D. & VERZICCO, R. 2011 Prandtl and Rayleigh number dependence of heat transport in high Rayleigh number thermal convection. *J. Fluid Mech.* **688**, 31–43.

STEVENS, R. J. A. M., VERZICCO, R. & LOHSE, D. 2010 Radial boundary layer structure and Nusselt number in Rayleigh–Bénard convection. *J. Fluid Mech.* **643**, 495–507.

SUGIYAMA, K., CALZAVARINI, E., GROSSMANN, S. & LOHSE, D. 2009 Flow organization in two-dimensional non-Oberbeck–Boussinesq Rayleigh–Bénard convection in water. *J. Fluid Mech.* **637**, 105–135.

SUGIYAMA, K., NI, R., STEVENS, R. J. A. M., CHAN, T.-S., ZHOU, S.-Q., XI, H.-D., SUN, C., GROSSMANN, S., XIA, K.-Q. & LOHSE, D. 2010 Flow reversals in thermally driven turbulence. *Phys. Rev. Lett.* **105**, 034503.

SUN, C., REN, L.-Y., SONG, H. & XIA, K.-Q. 2005 Heat transport by turbulent Rayleigh–Bénard convection in 1 m diameter cylindrical cells of widely varying aspect ratio. *J. Fluid Mech.* **542**, 165–174.

SUN, C. & XIA, K.-Q. 2005 Scaling of the Reynolds number in turbulent thermal convection. *Phys. Rev.* E **72**, 067302.

SUN, C. & ZHOU, Q. 2014 Experimental techniques for turbulent Taylor–Couette flow and Rayleigh–Bénard convection. *Nonlinearity* **27**, R89–R121.

VERZICCO, R. 2003 Turbulent thermal convection in a closed domain: viscous boundary layer and mean flow effects. *Eur. Phys. J.* B **35**, 133–141.

VERZICCO, R. & CAMUSSI, R. 2003 Numerical experiments on strongly turbulent thermal convection in a slender cylindrical cell. *J. Fluid Mech.* **477**, 19–49.

VERZICCO, R. & SREENIVASAN, K. R. 2008 A comparison of turbulent thermal convection between conditions of constant temperature and constant heat flux. *J. Fluid Mech.* **595**, 203–219.

WAGNER, S., SHISHKINA, O. & WAGNER, C. 2012 Boundary layers and wind in cylindrical Rayleigh–Bénard cells. *J. Fluid Mech.* **697**, 336–366.

WHITEHEAD, J. P. & DOERING, C. R. 2011 Ultimate state of two-dimensional Rayleigh–Bénard convection between free-slip fixed-temperature boundaries. *Phys. Rev. Lett.* **106**, 244501.

ZHOU, Q. 2013 Temporal evolution and scaling of mixing in two-dimensional Rayleigh–Taylor turbulence. *Phys. Fluids* **25**, 085107.

ZHOU, Q., HUANG, Y.-X., LU, Z.-M., LIU, Y.-L. & NI, R. 2016 Scale-to-scale energy and enstrophy transport in two-dimensional Rayleigh–Taylor turbulence. *J. Fluid Mech.* **786**, 294–308.

ZHOU, Q. & JIANG, L.-F. 2016 Kinetic and thermal energy dissipation rates in two-dimensional Rayleigh–Taylor turbulence. *Phys. Fluids* **28**, 045109.

ZHOU, Q., LIU, B.-F., LI, C.-M. & ZHONG, B.-C. 2012 Aspect ratio dependence of heat transport by turbulent Rayleigh–Bénard convection in rectangular cells. *J. Fluid Mech.* **710**, 260–276.

ZHOU, Q., SUGIYAMA, K., STEVENS, R. J. A. M., GROSSMANN, S., LOHSE, D. & XIA, K.-Q. 2011 Horizontal structures of velocity and temperature boundary layers in two-dimensional numerical turbulent Rayleigh–Bénard convection. *Phys. Fluids* **23**, 125104.

ZHOU, Q. & XIA, K.-Q. 2010 Measured instantaneous viscous boundary layer in turbulent Rayleigh–Bénard convection. *Phys. Rev. Lett.* **104**, 104301.

ZHOU, Q. & XIA, K.-Q. 2013 Thermal boundary layer structure in turbulent Rayleigh–Bénard convection in a rectangular cell. *J. Fluid Mech.* **721**, 199–224.

https://doi.org/10.1017/jfm.2017.19 Published online by Cambridge University Press